The final publication is available at

https://doi.org/10.1002/anie.202313101

Additional Information

Encapsulation of Palladium Carbide Subnanometric Species in Zeolite Boosts Highly Selective Semihydrogenation of Alkynes

Risheng Bai, Guangyuan He, Lin Li, Tianjun Zhang, Junyan Li, Xingxing Wang, Xiumei Wang, Yongcun Zou, Donghai Mei,* Avelino Corma,* and Jihong Yu*

Abstract: The selective hydrogenation of alkynes to alkenes is a crucial step in the synthesis of fine chemicals. However, the widely utilized palladium (Pd)-based catalysts often suffer from poor selectivity. In this work, we demonstrate a carbonization-reduction method to create palladium carbide subnanometric species within pure silicate MFI zeolite. The carbon species can modify the electronic and steric characteristics of Pd species by forming the predominant Pd—C_4 structure and, meanwhile, facilitate the desorption of alkenes by forming the Si—O—C structure with zeolite framework, as validated by the state-of-the-art characterizations and theoretical calculations. The developed catalyst shows superior performance in the selective hydrogenation of alkynes over mild conditions (298 K, 2 bar H_2), with 99 % selectivity to styrene at a complete conversion of phenylacetylene. In contrast, the zeolite-encapsulated carbon-free Pd catalyst and the commercial Lindlar catalyst show only 15 % and 14 % selectivity to styrene, respectively, under identical reaction conditions. The zeolite-confined Pd-carbide subnanoclusters promise their superior properties in semihydrogenation of alkynes.

Introduction

Alkenes, such as ethylene and styrene, are important chemical intermediates for the polymer, pharmaceutical, and pigment industries.[1] However, the presence of trace amounts of alkyne contaminants, such as acetylene and phenylacetylene, can frequently result in the deactivation alkene polymerization catalysts.[2] The selective hydrogenation of alkynes to their corresponding alkenes, while avoiding over-hydrogenation of alkenes to the undesired alkanes, is a crucial industrial process.[3] The exceptional capability of palladium (Pd) nanoparticles in activating hydrogen, makes it one of the most efficient active catalysts for this process, facilitating the reaction even at room temperature and atmospheric pressure.[4] However, surface hydrogen atoms have a tendency to migrate into the subsurface of Pd nanoparticles and lead to the formation of β-hydride species, which exhibit higher activity in the hydrogenation process than hydrogen species adsorbed on the Pd surfaces, leading to the over hydrogenation of alkynes.[5] In addition, the assembly of Pd atoms could influence the adsorption mode and desorption energy of the unsaturated reactants/intermediates, thus affecting the alkene selectivity.[6] The "site-isolated" and surface modification strategies, including the introduction of a second metal or metal oxide on Pd nanoparticles or the construction of Pd-based intermetallic compounds have proven to be effective approaches in optimizing the adsorption configurations and

[*] Dr. R. Bai, Dr. J. Li, X. Wang, Dr. Y. Zou, Prof. J. Yu
Department State Key Laboratory of Inorganic Synthesis and Preparative Chemistry, College of Chemistry
Jilin University
130012 Changchun (China)
E-mail: jihong@jlu.edu.cn

Dr. R. Bai, Prof. A. Corma
Instituto de Tecnología Química
Universitat Politècnica de València-Consejo Superior de Investigaciones Científicas
46022 Valencia (España)
E-mail: acorma@itq.upv.es

G. He, Prof. D. Mei
School of Materials Science and Engineering, State Key Laboratory of Separation Membranes and Membrane Processes
Tiangong University
300387 Tianjin (China)
E-mail: dhmei@tiangong.edu.cn

Dr. L. Li
Electron Microscopy Center
Jilin University
130012 Changchun (China)

Dr. T. Zhang
College of Chemistry and Materials Science
Hebei University
071002 Baoding (China)

Dr. X. Wang
Bruker (Beijing) Scientific Technology Co., Ltd.
100000 Beijing (China)

Dr. J. Li
Center for High-resolution Electron Microscopy (ChEM), School of Physical Science and Technology
ShanghaiTech University
201210 Shanghai (China)

Prof. J. Yu
International Center of Future Science
Jilin University
130012 Changchun (China)

[Escriba aquí]

desorption energies of the alkynes and alkenes, but suffer from high cost, complex preparation processes, and the use of toxic promoters (e.g., lead or sulfur in Lindlar catalysts).[7] Therefore, developing efficient Pd-based catalysts with high selectivity and activity, free of β-hydride, is a highly desired yet challenging target for semihydrogenation of alkynes.

It has been recognized that for alkyne hydrogenation reactions, positively charged Pd sites, such as Pd in the form of carbides or single atom catalysts that are anchored through Pd–C, Pd–O, or Pd–N bonds, can weaken the adsorption of alkene and lead to an increase in alkene selectivity.[8] Pérez-Ramírez and co-workers demonstrated that the Pd centers in the Pd/mpg–C_3N_4 catalyst exhibited partially positive charges and could adsorb ethylene molecules in a non-active configuration in the semihydrogenation of acetylene, resulting in the high ethylene selectivity.[9] However, the poor thermal stability, inferior recyclability, and unsuitability of single-atom catalysts for scaling up pose significant challenges for their widespread practical applications. Additionally, weak interactions between reactants and slow H_2 dissociation kinetics may hinder the hydrogenation reactivity, fueling ongoing efforts to synthesize electron-deficient Pd-based catalysts with appropriate adsorption/desorption energy and hydrogenation barriers for enhanced selectivity towards alkenes.

Zeolites, with well-defined microporous structures and excellent chemical and thermal stability are promising supports for confining metal clusters/nanoparticles.[10] Metallic species can be incorporated into zeolite crystals by means of ion-exchange, impregnation, zeolite shell-encaged method, ligand-stabilized method, precursor-protected method, etc. The zeolite matrix could efficiently suppress the aggregation of metal nanoparticles, and the uniform channels also exert control over the molecules, thereby affording selective product yields in various reactions.[11] Gong and co-workers achieved the high ethylene selectivity by using Pd@SOD catalyst through an uncontacted mechanism, where the H_2 is activated by the Pd in SOD zeolite, and then spills over the SOD surfaces to achieve the selective hydrogenation.[12]

In this work, with an aim to the development of efficient catalysts with positively charged Pd sites and optimized adsorption energy towards alkenes, we create subnanometric palladium carbide species in the pure siliceous MFI (silicalite-1, S-1) zeolite based on a direct carbonization-reduction strategy subjected to the hydrothermal crystallization (denoted as PdCx@S-1). The in situ formed carbon species, anchored inside the S-1 zeolite channels, could modify the steric and electronic characteristics of the incorporated Pd species, conferring an electron-lean nature to the Pd clusters. Meanwhile, the decoration of the zeolite framework with C can promote the desorption of the intermediate styrene and boost the hydrogen activation. Consequently, the PdCx@S-1 catalyst shows remarkable improvement in catalytic selectivity for the selective hydrogenation of phenylacetylene compared to the metallic Pd clusters confined in S-1 zeolite (Pd@S-1), achieving 99 % selectivity for styrene at complete conversion of phenyl-

acetylene under mild reaction conditions (298 K, 2 bar H_2) versus only 15 % selectivity for the Pd@S-1 catalyst.

Results and Discussion

Figure 1a illustrates the synthesis of zeolite-encapsulated PdCx@S-1 sample using the direct carbonization-reduction method. Firstly, Pd species were introduced into the silicalite-1 zeolite through a one-pot hydrothermal synthesis process, by using [Pd($NH_2CH_2CH_2NH_2$)$_2$]Cl$_2$ (Pden) as the Pd precursor. The resultant sample, denoted as Pden@S-1, was treated by the direct carbonization-reduction under H_2 atmosphere at 300 °C (Figures S1, S2). The PdCx species then were formed in situ inside the S-1 zeolite channels forming PdCx@S-1. As a comparison, Pd@S-1 containing metallic Pd species was prepared by first calcination in air at 550 °C to remove all organics, followed by reduction under H_2 atmosphere at 400 °C. All the Pd containing S-1 zeolite samples show characteristic X-ray diffraction (XRD) patterns of MFI topology (Figure S3). In addition, no visible plane diffraction peaks of the Pd metal nanoparticles can be detected, ascribing to the low loading amounts, ultrasmall sizes, and uniformly dispersion of Pd species. Inductively coupled plasma-optical emission spectroscopy (ICP-OES) analysis reveals that the Pd loadings of PdCx@S-1 and Pd@S-1 are similar, 0.90 wt% and 0.91 wt%, respectively (Table S1). Scanning electron microscopy (SEM) displays the coffin-like morphology and particle size of approximately 250 nm for both PdCx@S-1 and Pd@S-1 (Figure S4). Transmission electron microscopy (TEM) and C_s-corrected scanning TEM annular dark-field (STEM-ADF) images demonstrate that Pd species in PdCx@S-1 are distributed in the interior part of the zeolite crystals (Figure 1b–g and Figure S5), and the average particle size of Pd clusters is about 0.71 nm (Figure 1f), much smaller than the Pd species in Pd@S-1 (1.70 nm, Figure S6), implying that the carbonization-reduction process under H_2 atmosphere could effectively prevent the aggregation of Pd species. Besides, the Pd dispersion (percentage of accessible Pd species to the total number of Pd atoms) of PdCx@S-1 is higher than that of Pd@S-1 (51.7 vs. 45.2 %, Figure S7). C_s-corrected STEM-ADF images of PdCx@S-1 obtained along the [100] (Figure 1c, d) and [010] (Figure 1e, f) directions display the location of the Pd species within the sinusoidal channels of MFI.

Significantly, the high-resolution C_s-corrected STEM-ADF images reveal the presence of Pd clusters consisting of a few atoms and individual Pd atoms with a fine dispersion that are distinguishable with clarity (Figure 1g, h). Furthermore, the MFI framework structure is observed to be faithfully preserved upon Pd metal loading, as evidenced by C_s-corrected STEM-bright-field (BF) image of PdCx@S-1 (Figure 1i). The high-angle annular dark-field (HAADF)-STEM image and energy dispersive spectroscopy (EDS) element mappings indicate that Si, O and Pd elements in both PdCx@S-1 and Pd@S-1 are homogeneously distributed throughout the zeolite crystals (Figure 1j and Figure S8).
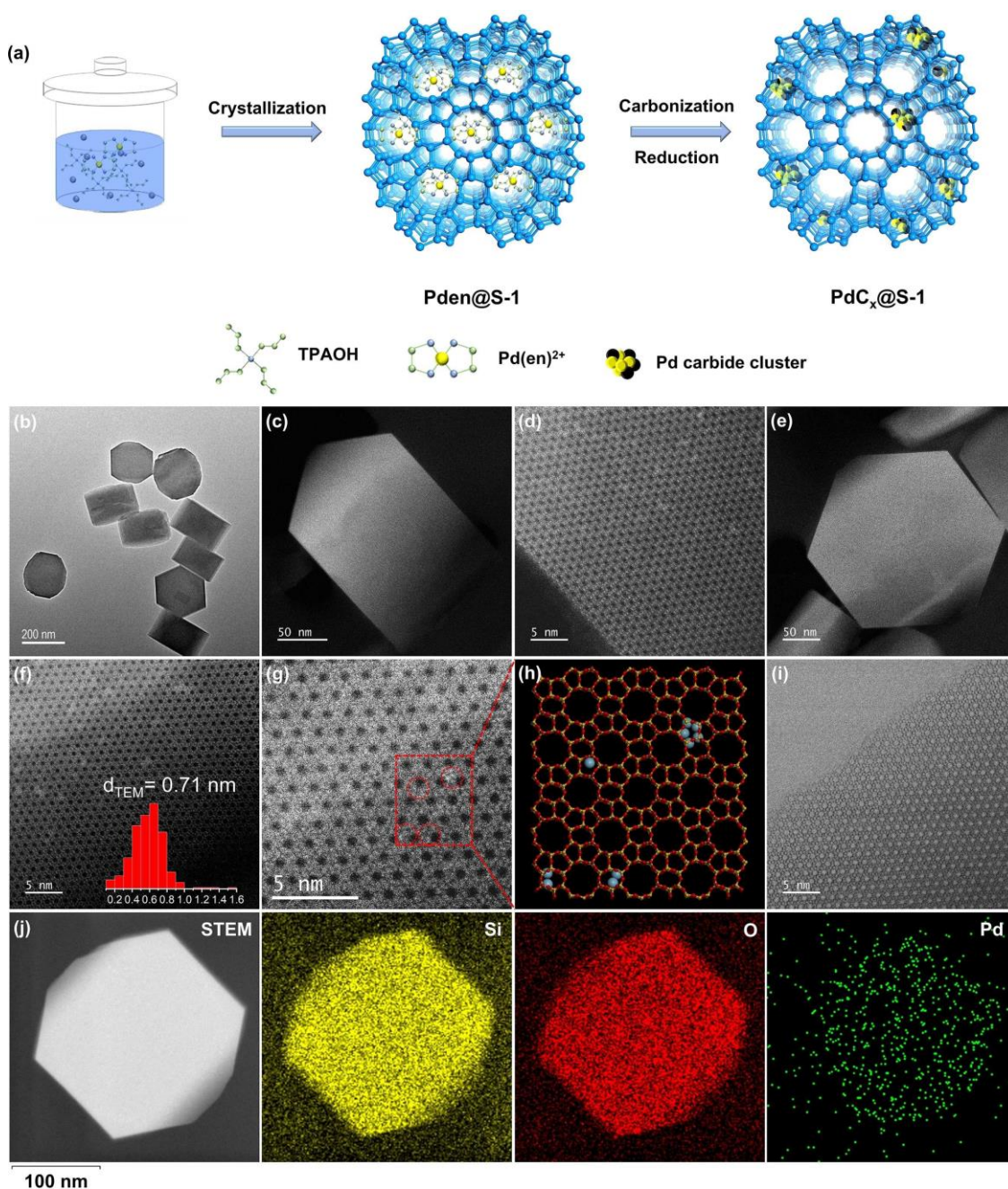
Figure 1. (a) The schematic illustration of the fabrication of zeolite-encapsulated PdC$_x$@S-1 by carbonization-reduction subjected to in situ hydrothermal crystallization. (b) TEM image of PdC$_x$@S-1. C$_s$-corrected STEM-ADF images of PdC$_x$@S-1 along (c, d) [100] and (e, f) [010]. (g) C$_s$-corrected STEM-ADF image of PdC$_x$@S-1. (h) Schematic image of the location of Pd species in PdC$_x$@S-1. (i) C$_s$-corrected STEM-BF image of PdC$_x$@S-1. (j) HAADF-STEM image and elemental mappings for elements of Si, O, and Pd in PdC$_x$@S-1. Insert in (f): the size distribution of Pd species in PdC$_x$@S-1.

Thermalgravimetric analysis (TGA) shows that PdC$_x$@S-1 exhibits a weight loss of 4.5 wt% within the temperature range of 100 to 600'C, revealing the presence of the carbon species in the sample (Figure S9), as confirmed by the Fourier transform-infrared (FT-IR) (Figure S10) and elemental CHN analysis results (Table S2).[13] N$_2$ and Ar adsorption-desorption results reveal that PdC$_x$@S-1 sample exhibits a lower N$_2$/Ar adsorption volume than the Pd@S-1 in the relative pressure region of P/P$_0$ < 0.1, showing a lower micropore volume (Figure 2a and Figure S11), which is also supported by the cumulative pore volume (Figure 2b), pore size distribution (Figure S12), and the textural property analyses (Table S1). Considering the good crystallinity of PdC$_x$@S-1 as determined by the XRD patterns, the lower micropore volume of PdC$_x$@S-1 may be ascribed to the partial blockage of the microporous channels by the formed PdC$_x$ species.
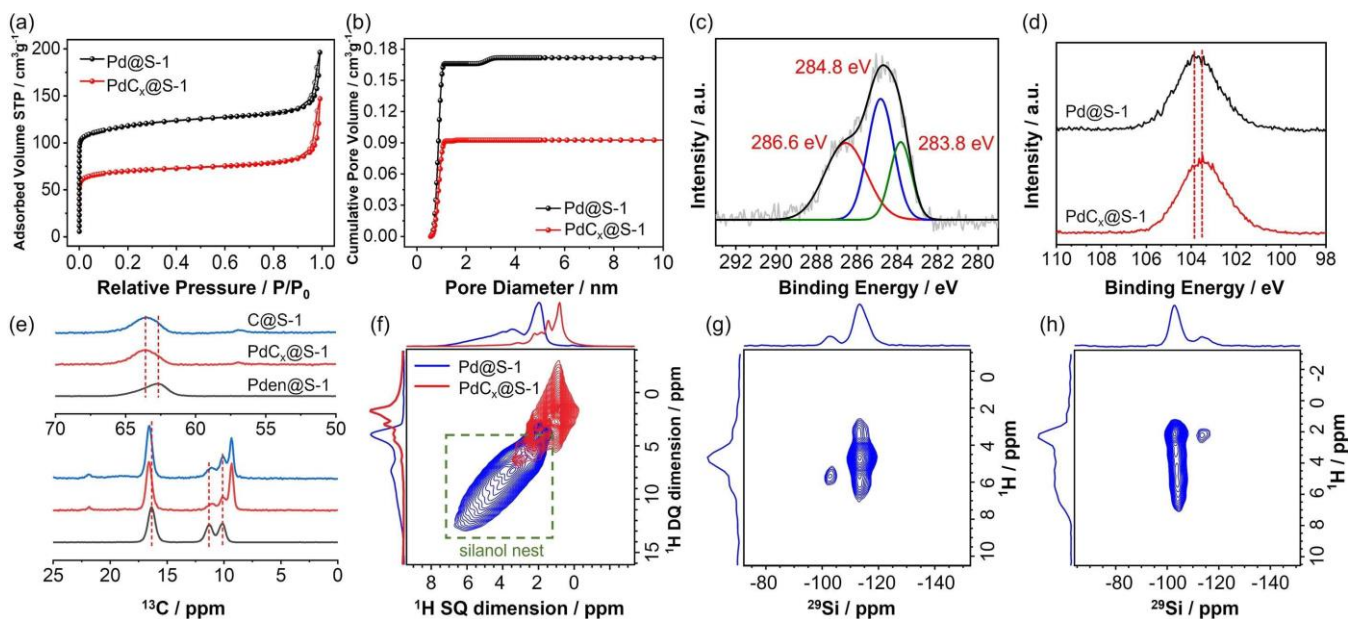
Figure 2. (a) N_2 adsorption/desorption isotherms and (b) cumulative pore volume curves of $PdC_x@S-1$ and $Pd@S-1$. (c) XPS spectrum of C 1s in $PdC_x@S-1$. (d) XPS spectra of Si 2p in $PdC_x@S-1$ and $Pd@S-1$. (e) ^1H-^{13}C CP MAS NMR spectra. (f) 2D ^1H-^1H DQ-SQ MAS NMR spectra. ^1H-^{29}Si HETCOR spectra of (g) $PdC_x@S-1$ and (h) $Pd@S-1$.

To gain additional insights into the structural composition of the carbon species, X-ray photoelectron spectroscopy (XPS) measurements were carried out. Figure 2c illustrates the high-resolution C 1s spectrum of $PdC_x@S-1$, which can be fitted with three components at around 283.8, 284.8, and 286.6 eV, ascribed to the carbide phase (palladium carbide, in this case), C–C/C–H (sp^3), and C–O bonds, respectively, in accordance with previous studies.[8a,14] Additionally, Si 2p XPS spectrum of $PdC_x@S-1$ shows the peak at the binding energy of 103.5 eV, which is lower than that of the $Pd@S-1$, implying a transfer of electron density from the carbon species to the silicon atoms in the $PdC_x@S-1$ sample (Figure 2d).

To assess the impact of the carbonation process on the organic template TPA^+ and ethylenediamine wrapped in S-1 zeolite crystals during crystallization, $C@S-1$ was synthesized as a comparison sample by following the same preparation procedure as the $PdC_x@S-1$, but without introducing Pd (Figures S13, S14). Solid state ^1H-^{13}C cross-polarization (CP) MAS NMR spectra (Figure 2e and Figures S15, S16) reveal the formation of new carbon species (9.42, 21.93, and 57.02 ppm) and the maintenance of some TPA^+ molecules after the carbonization process (10.18, 11.20, 16.64, and 63.62 ppm). Furthermore, O_2 temperature programmed oxidation (O_2-TPO) was performed to determine the organic species in the prepared catalysts (Figure S17). The oxidation of tetrapropylammonium cations located in the $Pden@S-1$ occurs at approximately 340°C, accompanied by a small peak at 430 C. In comparison to the carbonized $C@S-1$ that shows the major oxidation peak at 393°C, the $PdC_x@S-1$ exhibits two peaks at 300 and 415°C, which can be ascribed to the carbon species interacting with Pd clusters and Si atoms in the zeolite skeleton, respectively, demonstrating the structural change of the organics in the zeolite crystals after the carbonization process under H_2 atmosphere.

^1H MAS NMR spectroscopy was employed to elucidate the structure and local chemical interactions of hydrogen atoms in both organics and silanol groups (Figure S18). In principle, the peaks with a chemical shift of around 1.9, 2.2, and 6.6 ppm can be ascribed to the isolated Si–OH without H-bonds, vicinal or geminal Si–OH, and H-bonded silanol groups, respectively, for both $PdC_x@S-1$ and $Pd@S-1$.[15] The peaks at 0.87 and 1.51 ppm in $PdC_x@S-1$ can be assigned to the H_γ and H_β of TPA^+, respectively, further confirming the presence of the organic species in the sample. Figure 2f depicts the 2D ^1H-^1H DQ-SQ MAS NMR spectra of $PdC_x@S-1$ and $Pd@S-1$ samples. In comparison to the $Pd@S-1$, $PdC_x@S-1$ shows the absence of correlation signal ranging from 3.0 to 7.0 ppm, which is linked to silanol nests, indicating that the $PdC_x@S-1$ contains fewer Si–OH groups than the $Pd@S-1$. However, following the complete removal of the organic species from $PdC_x@S-1$ through calcination in air, the ^1H-^1H DQ-SQ spectrum exhibits notable silanol nest signals spanning from 3.0 to 7.0 ppm (Figure S19). Above observations suggest that the carbonization process for the $PdC_x@S-1$ may impede the formation of isolated Si–OH by fostering the Si–O–C structure.

Solid state ^{29}Si MAS NMR spectra of $PdC_x@S-1$ and $Pd@S-1$ show the signals at –102 and –112 ppm, which can be attributed to the Q^3 and Q^4 silicon atoms, respectively (Figure S20a). Notably, the signal in ^1H-^{29}Si CP MAS NMR spectrum is similar to that in ^{29}Si MAS NMR spectrum, in which –112 ppm signal is dominant, implying that most of the silicon atoms are tetrahedral coordination in the form of $Si(OSi)_4$ or $Si(OSi)_3(OC)$ (Figure S20b). Conversely, as for the $Pd@S-1$, the signal of –102 ppm is dramatically enhanced in ^1H-^{29}Si CP MAS NMR spectrum, suggesting

that some Si atoms in the S-1 crystals are connected with three Si atoms and one hydroxyl group, that is, Si(OH)-(OSi)$_3$. 2D ^{1}H-^{29}Si HETCOR spectra, which exploit the dipolar interactions between ^{1}H and ^{29}Si nuclei, further clarify the through-space proximity between different structural fragments in PdC$_x$@S-1 and Pd@S-1 (Figure 2g–h). ^{1}H-^{29}Si HETCOR spectrum of PdC$_x$@S-1 displays a strong correlation between Q^4 silicon atoms and the hydrogen-bonded Si–OH groups. In contrast, the HETCOR spectrum of Pd@S-1 shows strong correlation associated with framework Q^3 sites and vicinal Si–OH groups, confirming their spatial proximity. Moreover, the water adsorption measurements at 298 K further reveal that PdC$_x$@S-1 is more hydrophobic than the Pd@S-1, with a water absorption of 4.4 vs. 5.8 wt% at 85% humidity (Figure S21). These results suggest that the presence of carbon species in zeolite crystals could effectively eliminate the isolated Si–OH groups by forming the Si–O–C structure, thus tuning the local microenvironment of the Pd species in PdC$_x$@S-1 catalyst and may endow influence on the catalytic performances.

The microenvironment and chemical state of Pd species in PdC$_x$@S-1 and Pd@S-1 samples were investigated by XPS and X-ray absorption fine structure (XAFS) measurements. Figure 3a depicts the Pd 3d$_{5/2}$ XPS spectra of Pd@S-1 showing the bands at 336.4 and 335.5 eV. The peak with higher binding energy (336.4 eV) in the PdC$_x$@S-1 spectrum signifies the presence of Pd species with positive charge density in the sample.[8a]

The Pd K-edge X-ray absorption near-edge structure (XANES) spectra of PdC$_x$@S-1 and Pd@S-1, as well as the corresponding references, are shown in Figure 3b. Both the white line intensity peak and the absorption edge of PdC$_x$@S-1 and Pd@S-1 are positioned between PdO and Pd foil, indicating that the Pd species are positively charged. The increased valence state of Pd is due to partial oxidation

in air and the interactivity between Pd and O of the zeolite skeleton. Notably, the white line intensity of PdC$_x$@S-1 is similar to that of the PdO, suggesting the strong interaction between Pd and C species, which agrees well with the XPS result. The Fourier-transformed (FT) k^2-weighted extended X-ray absorption fine structure (EXAFS) spectrum of PdC$_x$@S-1 reveals a sharp peak located at 1.51 Å, which can be associated to the Pd–C contributions (Figure 3c), indicating that the Pd–C species dominates the Pd species status. For the Pd@S-1, the major peak located at 2.44 Å, accompanied by a small peak located at 1.53 Å, that can be attributed to the contributions of Pd–Pd and Pd–O, respectively, implying that the metallic Pd species is dominant. Moreover, wavelet transform (WT) was also employed for EXAFS analysis to identify scattering atoms and offer resolutions in both R-space and k-space (Figure 3e–h). The WT EXAFS spectrum of PdC$_x$@S-1 shows that the WT intensity maximum near 5.7 Å^{-1} in k-space is resolved at 1.4 Å in R-space, which can be ascribed to Pd–C coordination. The Pd@S-1 demonstrates a maximum intensity peak at 10.0 Å^{-1} in k-space and at 2.3 Å in R-space, which is associated with the Pd–Pd coordination, suggesting the dominance of metallic Pd species. Above mentioned results substantiate the assignment of the main peak at 1.4 Å in PdC$_x$@S-1 to Pd–C bonding.

Least-squares EXAFS fitting analysis was also conducted to reveal quantitative structures of Pd moiety in both PdC$_x$@S-1 and Pd@S-1. The best-fitting results show that the Pd atom in PdC$_x$@S-1 is coordinated with four C atoms (coordination number (CN) 4.2) at distances of 2.03 Å (Figure S22 and Table S3), suggesting the formation of Pd–C$_4$ structures. In addition, the fitting results of EXAFS reveal the presence of a Pd–O shell (R 2.05 Å, CN 1.7) and a Pd–Pd shell (R 2.72 Å, CN 4.2) in Pd@S-1. The lower coordination number of Pd–Pd in PdC$_x$@S-1 indicates
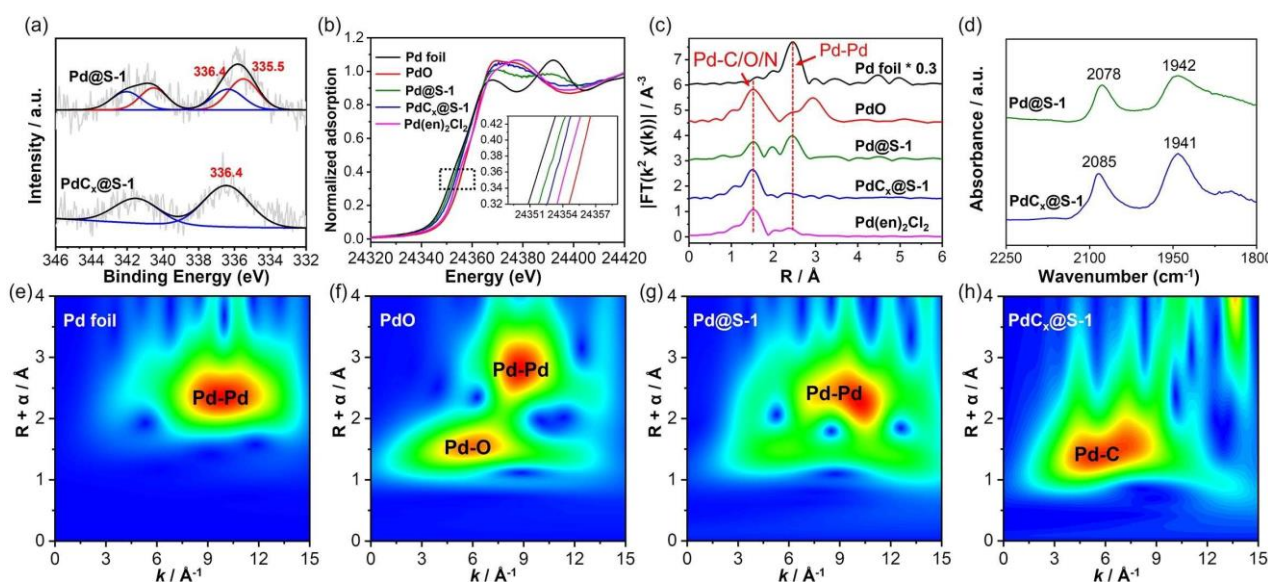

Figure 3. (a) Pd 3d XPS spectra of PdC$_x$@S-1 and Pd@S-1. (b) Pd K-edge XANES and (c) EXAFS oscillations of Pd foil, PdO, PdC$_x$@S-1, Pd@S-1, and Pd(en)$_2$Cl$_2$. (d) In situ CO-DRIFTS spectra of PdC$_x$@S-1 and Pd@S-1. WT for the k^2-weighted EXAFS signals of (e) Pd foil, (f) PdO, (g) Pd@S-1, and (h) PdC$_x$@S-1.

a smaller size of Pd clusters compared to Pd@S-1, consistent with the findings from TEM. In addition, the electronic states of Pd species in PdC$_x$@S-1 and Pd@S-1 were also investigated by in situ diffuse reflectance infrared Fourier transform spectroscopy (DRIFTS) using CO as a probe molecule (Figure 3d). The peak corresponding to linear-adsorbed CO on Pd species shifts from 2078 cm^{-1} in Pd@S-1 to 2085 cm^{-1} in PdC$_x$@S-1, implying that the Pd species in PdC$_x$@S-1 possess a positive charge of density (as determined from the XPS and XAS results), and/or the dipolar coupling effect.[16] The peaks at 1941 cm^{-1} and 1942 cm^{-1} in the CO-DRIFTS spectra can be ascribed to the bridged-CO molecules on Pd species, suggesting the presence of clusters or nanoparticles in the prepared two Pd catalysts. In addition, Cl 2p XPS spectra and N 1s XPS spectra imply that the Pd species in PdC$_x$@S-1 may not coordinated with N/Cl atoms (Figures S23, S24).

We conducted an evaluation of the catalytic performance in the semihydrogenation of alkynes using PdC$_x$@S-1 and Pd@S-1 catalysts, with a focus on achieving high alkene selectivity at high conversion levels. In the semihydrogenation of phenylacetylene with H$_2$ as the reductant at 25°C, PdC$_x$@S-1 exhibits lower activity than Pd@S-1 (turnover frequency, 513 vs. 1032 h^{-1}), while the styrene selectivity over PdC$_x$@S-1 catalyst is 99% at the full conversion of the reactant after reacting for 4 h, which is significantly superior than that of the Pd@S-1 counterpart (15%), the impregnated PdC$_x$/S-1 (0%) and Pd/S-1 (0%), as well as the commercial Pd/C (0%) and Lindlar (14%) catalysts (Figure 4a–c and Figures S25–S29). Notably, the phenylacetylene (4.297×7.572 Å) could penetrate the pores of both PdC$_x$@S-1 and Pd@S-1 in a direction parallel to the MFI channels and undergo the hydrogenation reaction over the

Pd species encapsulated in the pores (Figure S12). When extending the reacting time to 6 h, the selectivity to styrene slightly decreases to 97% over PdC$_x$@S-1 catalyst, while that over the Pd@S-1 catalyst drops to �0% (Figure S30). After five cycles, the PdC$_x$@S-1 catalyst still shows the styrene selectivity of 96% at the full conversion of phenylacetylene (Figure 4d), and the crystallinity of zeolite sheath and the Pd species remain almost unchanged, as evidenced by XRD, TEM, and XPS measurements (Figures S31–S33), indicating the stability of the catalyst for semihydrogenations. In addition, the kinetics of phenylacetylene semihydrogenation and styrene hydrogenation were investigated. The analyses of the initial reaction rates at different temperatures lead to the construction of Arrhenius plots depicting the relationship between ln$r$ and 1/T (Figure 4e), yielding apparent activation energies of 30.1 kJ mol^{-1} for phenylacetylene semihydrogenation and 58.8 kJ mol^{-1} for styrene hydrogenation. Furthermore, the Eyring-Polanyi approximation (Figure S34) gives enthalpies of activation for phenylacetylene and styrene are 27.5 vs. 56.2 kJ mol^{-1}, respectively; and the decrease in entropy of phenylacetylene is remarkably higher than that of the styrene (-165.5 vs. -84.5 J mol^{-1} K^{-1}), indicating that PdC$_x$@S-1 favors the hydrogenation of phenylacetylene over styrene. While for the Pd@S-1, the apparent activation energies were found to be 31.0 kJ mol^{-1} for phenylacetylene semihydrogenation and 28.8 kJ mol^{-1} for styrene hydrogenation (Figure S35); the latter one exhibits even greater ease.

Considering the impact of the carbonization process which prejudices the generation of isolated silanol group by forming the Si−O−C structure in the PdC$_x$@S-1, it is anticipated that the weakened H-π interaction between the Si−OH groups and the alkene moieties will result in reduced interaction between the PdC$_x$@S-1 catalyst and alkenes.[17] We carried out in situ FT-IR study and phenylacetylene/styrene temperature programmed desorption (TPD) on PdC$_x$@S-1 and Pd@S-1 to obtain a deeper understanding of the mechanism (Figure 5). The signals in FT-IR spectra at 2108 cm^{-1} can be ascribed to the stretching vibration of C�C and the signal at 1630 cm^{-1} is related to the C=C group. Compared to Pd@S-1, PdC$_x$@S-1 exhibits lower desorption temperatures for both phenylacetylene and styrene molecules, revealing a weaker interaction between the substrates and PdC$_x$@S-1 (Figure 5a–d), probably responsible for the high styrene selectivity.

Figures 5e and 5f depict the phenylacetylene and styrene TPD spectra of the two catalysts. The desorption peak of phenylacetylene over PdC$_x$@S-1 is located at 209°C, which is lower than over the Pd@S-1 (241°C), but increases the amount of adsorption. Notably, the styrene desorption behavior over the PdC$_x$@S-1 occurs at temperatures of 136 and 212°C, which are lower than those observed for Pd@S-1 (at 141 and 233°C). This indicates that PdC$_x$@S-1 shows a lower affinity for styrene compared to Pd@S-1, which would be attributed to the modifications in the electrical characteristics of the Pd species and a reduction in the silanol groups resulting from the incorporated carbon species, thus contributing to the substantial improvement in alkene selectivity in the phenylacetylene hydrogenation.
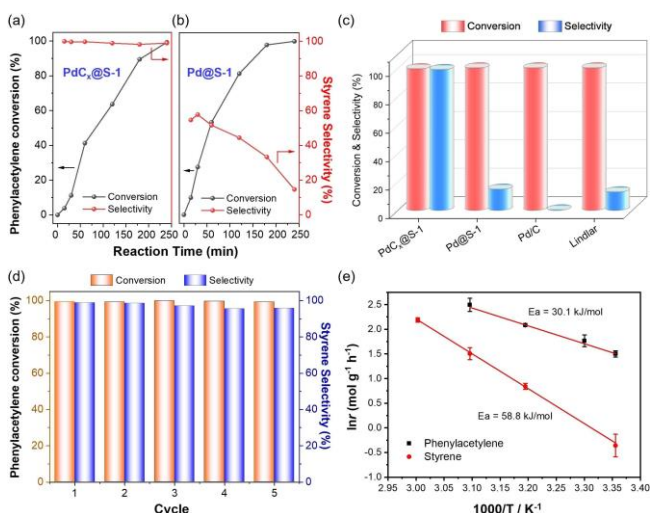

Figure 4. The conversion of phenylacetylene and selectivity of styrene versus time over (a) PdC$_x$@S-1 and (b) Pd@S-1. (c) Comparison of phenylacetylene conversion and styrene selectivity over various catalysts. Reaction conditions: 1 mmol phenylacetylene, Pd 0.0846 mol%, 298 K, 2 bar H$_2$, 2 mL ethanol. (d) Stability test of PdC$_x$@S-1. (e) Arrhenius plots of the semihydrogenation of phenylacetylene and hydrogenation of styrene over PdC$_x$@S-1.
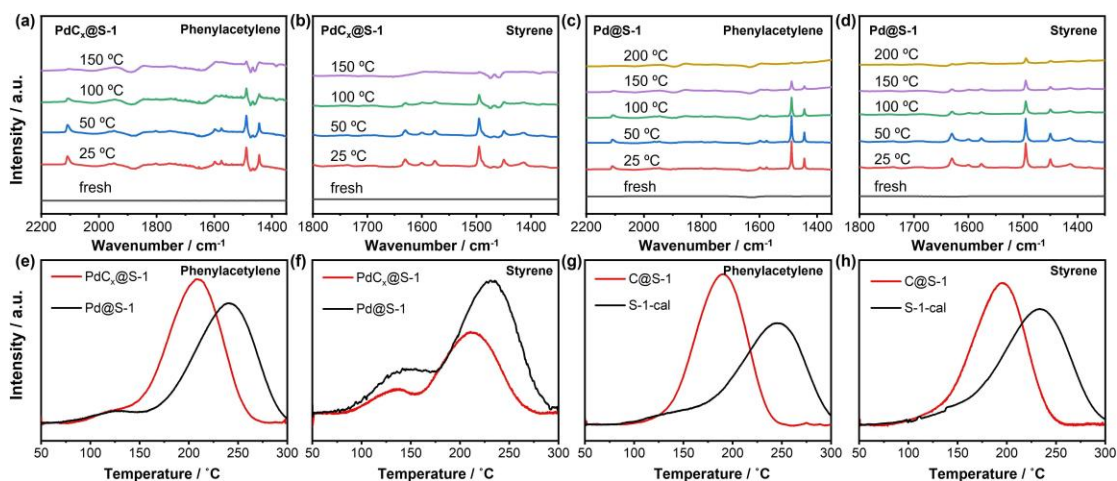
Figure 5. In situ FT-IR spectra of adsorbed phenylacetylene and styrene on (a, b) PdC$_x$@S-1 and (c, d) Pd@S-1. (e, g) Phenylacetylene-TPD and (f, h) styrene-TPD spectra over different catalysts.

In order to further evaluate the effect of Pd and PdC$_x$ species and to unravel the role of the porous zeolite framework in the semihydrogenations, two additional Pd-free samples, C@S-1 and S-1-cal, were synthesized for comparison (Figures S13, S14 and Figures S36–S39). As shown in Figures 5g and 5h, the TPD spectra of C@S-1 show lower adsorption amount and lower desorption temperatures for both phenylacetylene (190 vs. 247°C) and styrene (196 vs. 234 C) than those of the S-1-cal, indicating that the incorporation carbon species could decrease the binding energy of phenylacetylene/styrene to the silicate zeolite frameworks, thus providing further confirmation of the positive effect exerted by the formed carbon species.

H$_2$-D$_2$ isotopic exchange, H$_2$-DRIFTS, and H$_2$-TPD were performed to provide a more in-depth understanding of the interaction between the Pd species and H$_2$. Figure S40 indicates that the PdC$_x$@S-1 catalyst shows slightly higher activity than the Pd@S-1 in activating H$_2$. H$_2$-DRIFTS spectrum of PdC$_x$@S-1 exhibits a series of IR bands ranging from 2970 to 3900 cm^{-1} and an IR band at 2038 cm^{-1}, corresponding to different stretching vibrations of hydroxyls and Pd–H species, respectively, providing strong evidence for the heterolytic dissociation of dihydrogen over the PdC$_x$@S-1 (Figure S41). It is noted that for the Pd@S-1, large silanol group signals and little Pd–H signal can be observed, suggesting that after the activation of H$_2$ on the Pd species, surface hydroxyl groups can be formed through hydrogen spillover processes. The band at 2355 cm^{-1} due to Pd–H$_2$ can be observed over the PdC$_x$@S-1, indicating an easier formation of Pd–H$_2$ on the PdC$_x$ species in PdC$_x$@S-1 than the Pd@S-1. In addition, H$_2$-TPD analyses show that the PdC$_x$@S-1 catalyst demonstrates higher H$_2$ desorption temperature and greater uptake of H$_2$ compared to the Pd@S-1 counterpart, implying that the Pd species with a positive density of charge is adept at activating the H$_2$ molecules, thus facilitating the hydrogenation reactions (Figure S42). Notably, the Pd-free C@S-1 sample also demonstrates a slightly higher capability for interacting with H$_2$ compared to the S-1-cal counterpart. This observation

suggests the advantages conferred by the formed carbon species through the carbonization process (Figure S42b).

To understand the superior selectivity of styrene over PdC$_x$@S-1, first principles density functional theory (DFT) calculations of semihydrogenation of phenylacetylene over PdC$_x$@S-1 and Pd@S-1 catalysts were carried out (Figure S43). The complete reaction energy profiles and corresponding structures are given in Figures S44–S47. As noted, although hydrogenation of phenylacetylene over both catalysts is highly exothermic, the calculated activation barrier for the key step, i.e., the hydrogenation barrier of the formed styrene over the PdC$_x$@S-1 is 114.8 kJ mol^{-1}, which is larger than its desorption energy of 66.7 kJ mol^{-1}, suggesting that the formed styrene prefers to desorb instead of being further hydrogenation to ethylbenzene (Figure 6 and Table S4). While on the Pd@S-1, the styrene hydrogenation barrier is only 41.4 kJ mol^{-1}, which is significantly less than its desorption energy of 101.5 kJ mol^{-1}. Thus, the formed styrene will be further hydrogenated instead of desorption. This indicates that, compared to Pd@S-1, the dominant
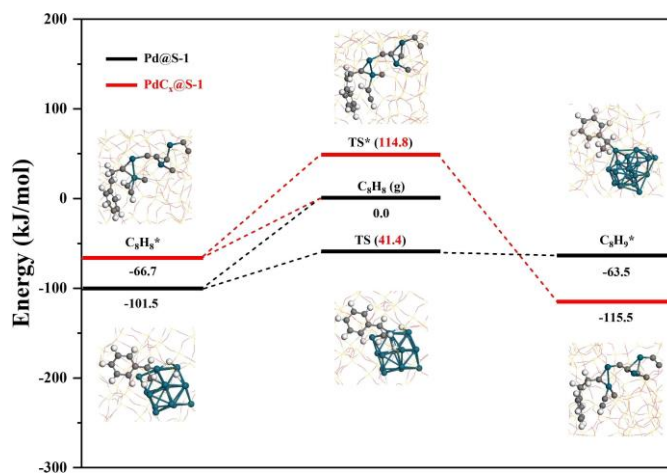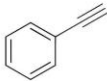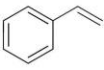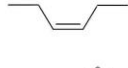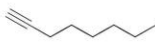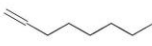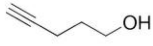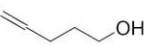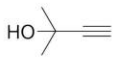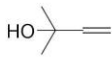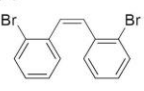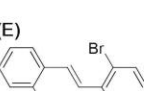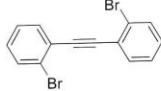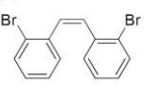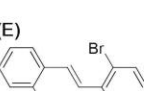

Figure 6. Hydrogenation of styrene over Pd@S-1 and PdC$_x$@S-1.

Table 1: Semihydrogenation of various alkynes.[a]

Entry	Catalysts	Substrate	Product	Time/h	Conversion/%	Selectivity/%
1	PdC$_x$@S-1	phenylacetylene	styrene	4	>99	>99
2	Pd@S-1			4	>99	15
3	PdC$_x$/S-1			4	>99	0
4	Pd/S-1			4	>99	0
5	Pd/C			4	>99	0
6	Lindlar			4	>99	14
7	PdC$_x$@S-1	2-hexyne	(Z)	2	>99	>99 (Z:E = 99:1)
8	Pd@S-1		(E)	2	>99	0
9	PdC$_x$@S-1	1-octyne	1-octene	7	>99	90
10	Pd@S-1			7	>99	2
11	PdC$_x$@S-1	4-pentyn-1-ol	4-penten-1-ol	5	>99	88
12	Pd@S-1			5	>99	0
13	PdC$_x$@S-1	3,3-dimethyl-1-butyne	3,3-dimethyl-1-butene	2	>99	95
14	Pd@S-1			2	>99	67
15	PdC$_x$@S-1	2-methyl-3-butyn-2-ol	2-methyl-3-buten-2-ol	2	>99	90
16	Pd@S-1			2	>99	2
17[b]	PdC$_x$@S-1	bis(2-bromophenyl)acetylene	(Z)	24	0	-
18[b]	Pd@S-1			24	0	-
19[b]	PdC$_x$/S-1		(E)	12	36	>99 (Z:E = 99:1)
20[b]	Pd/S-1			12	40	>99 (Z:E = 99:1)

[a] Reaction conditions: 1.0 mmol substrate, Pd 0.0846 mol%, 2 mL ethanol, 298 K, 2 bar H_2. [b] 0.2 mmol substrate.

reaction path over PdC$_x$@S-1 shifts from the subsequent styrene hydrogenation to its desorption. Clearly, the high selectivity for styrene in the semihydrogenation of phenylacetylene over PdC$_x$@S-1 is expected, which confirms our experimental observation. Figure 7 shows the electronic density differences of the styrene over PdC$_x$@S-1 and Pd@S-1 catalysts. Compared to PdC$_x$@S-1, more electronic density accumulated (rich) indicates the stronger interaction between styrene and Pd nanocluster over the Pd@S-1, suggesting the strongly bound styrene will be further hydrogenated instead of desorption. On the other hand, the Pd of PdC$_x$@S-1 is positively charged with the Bader charge of + 0.39 $|e|$ (the Pd atoms are almost neutral (+ 0.04 $|e|$) in Pd@S-1), implying the weaker interaction between styrene and the carbonized palladium species, which leads to the
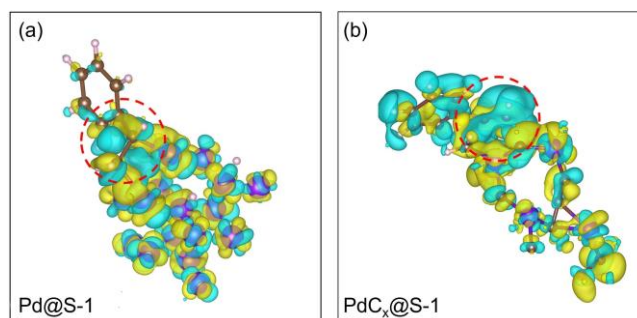

Figure 7. Electronic density differences for styrene over (a) Pd@S-1 and (b) PdC$_x$@S-1. The yellow and blue regions indicate electron accumulation and depletion, respectively.

facile desorption of styrene, resulting in higher styrene selectivity.[9]

As shown in Table 1, the distinctive catalytic behaviors of PdC$_x$@S-1 could be adapted to the semihydrogenation of a broad substrate scope of alkynes, except for bis(2-bromophenyl)acetylene—a voluminous molecule with dimensions 7.089×10.174 Å, beyond the accommodation capacity of the MFI structure's pores. Neither PdC$_x$@S-1 nor Pd@S-1 exhibited discernible catalytic activity toward the alkyne functionality within bis(2-bromophenyl)acetylene, even with extended reaction times up to 24 h. In contrast, the impregnated Pd/S-1 catalyst, featuring Pd nanoparticles of approximately 8.5 nm, achieved a 40 % conversion of bis(2-bromophenyl)acetylene at 12 h under identical reaction conditions. Hence, the elevated alkene selectivity observed with the PdC$_x$@S-1 catalyst in the selective hydrogenation of alkynes can be attributed to facile desorption of the resulting alkenes, rather than the uncontacted hydrogenation behavior.[12] Significantly, for alkynes with hydrophilic alkynyl substituents, such as hydroxyl groups, the PdC$_x$@S-1 catalyst demonstrates substantially improved alkene selectivity over Pd@S-1, which may greatly benefit from the encapsulated carbon species that decorates both the Pd species and the silanol moiety of the zeolite support, bringing zeolite support with the gift of hydrophobicity, thus promoting the desorption of the alkene intermediates and improving the selectivities.

Conclusion

In summary, we developed a facile carbonization-reduction strategy for encapsulating palladium carbide into purely silicious MFI zeolites. Detailed NMR, XAS, XPS, and CO-DRIFTS measurements suggested the formation of PdC$_x$ structures and revealed the positively charged Pd species. The PdC$_x$@S-1 catalyst exhibited robust catalytic performance, achieving a high selectivity of 99 % towards styrene in the complete conversion of phenylacetylene, and showed good catalyst stability and broad substrate compatibility under mild reaction conditions (298 K, 2 bar of H$_2$). Through a combination of experimental evidence and the theoretical calculations, the subnanometric PdC$_x$ species and the reduced silanols, through the formation of Si—O—C structure, contribute to facilitating H$_2$ activation and styrene desorption. Thereby, the rate-determining step is shifted from subsequent styrene hydrogenation to its desorption, thus leading to a significantly improved alkene selectivity in the selective alkyne hydrogenation reactions. Our findings provide a significant advancement in the development of high-performance catalysts for semihydrogenation reactions.

Conflict of Interest

The authors declare no conflict of interest.

Data Availability Statement

The data that support the findings of this study are available from the corresponding author upon reasonable request.

[1] a) A. Corma, *Chem. Rev.* **2014**, *114*, 1545–1546; b) M. Crespo-Quesada, F. Cárdenas-Lizana, A.-L. Dessimoz, L. Kiwi-Minsker, *ACS Catal.* **2012**, *2*, 1773–1786; c) M. Eggersdorfer, D. Laudert, U. Létinois, T. McClymont, J. Medlock, T. Netscher, W. Bonrath, *Angew. Chem. Int. Ed.* **2012**, *51*, 12960–12990.

[2] Y. Jin, A. K. Datye, E. Rightor, R. Gulotty, W. Waterman, M. Smith, M. Holbrook, J. Maj, J. Blackson, *J. Catal.* **2001**, *203*, 292–306.

[3] a) G. Vilé, D. Albani, N. Almora-Barrios, N. López, J. Pérez-Ramírez, *ChemCatChem* **2016**, *8*, 21–33; b) F. Huang, M. Peng, Y. Chen, X. Cai, X. Qin, N. Wang, D. Xiao, L. Jin, G. Wang, X. D. Wen, H. Liu, D. Ma, *J. Am. Chem. Soc.* **2022**, *144*, 18485–18493.

[4] a) K. Choe, F. Zheng, H. Wang, Y. Yuan, W. Zhao, G. Xue, X. Qiu, M. Ri, X. Shi, Y. Wang, G. Li, Z. Tang, *Angew. Chem. Int. Ed.* **2020**, *59*, 3650–3657; b) A. Borodziński, *Catal. Lett.* **1999**, *63*, 35–42.

[5] a) D. Teschner, J. Borsodi, A. Wootsch, Z. Révay, M. Hävecker, A. Knop-Gericke, S. D. Jackson, R. Schlögl, *Science* **2008**, *320*, 86–89; b) C. Riley, S. Zhou, D. Kunwar, A. De La Riva, E. Peterson, R. Payne, L. Gao, S. Lin, H. Guo, A. Datye, *J. Am. Chem. Soc.* **2018**, *140*, 12964–12973; c) A. L. Bugaev, O. A. Usoltsev, A. A. Guda, K. A. Lomachenko, I. A. Pankin, Y. V. Rusalev, H. Emerich, E. Groppo, R. Pellegrini, A. V. Soldatov, J. A. van Bokhoven, C. Lamberti, *J. Phys. Chem. C* **2018**, *122*, 12029–12037.

[6] a) Y. Liu, B. Wang, Q. Fu, W. Liu, Y. Wang, L. Gu, D. Wang, Y. Li, *Angew. Chem. Int. Ed.* **2021**, *60*, 22522–22528; b) S. K. Kim, C. Kim, J. H. Lee, J. Kim, H. Lee, S. H. Moon, *J. Catal.* **2013**, *306*, 146–154.

[7] a) N. López, C. Vargas-Fuentes, *Chem. Commun.* **2012**, *48*, 1379–1391; b) Q. Feng, S. Zhao, Q. Xu, W. Chen, S. Tian, Y. Wang, W. Yan, J. Luo, D. Wang, Y. Li, *Adv. Mater.* **2019**, *31*, e1901024; c) J. Osswald, R. Giedigkeit, R. E. Jentoft, M. Armbrüster, F. Girgsdies, K. Kovnir, T. Ressler, Y. Grin, R.

Schlögl, *J. Catal.* **2008**, *258*, 210–218; d) L. Zhao, X. Qin, X. Zhang, X. Cai, F. Huang, Z. Jia, J. Diao, D. Xiao, Z. Jiang, R. Lu, N. Wang, H. Liu, D. Ma, *Adv. Mater.* **2022**, *34*, e2110455.

[8] a) Y. Liu, F. Fu, A. McCue, W. Jones, D. Rao, J. Feng, Y. He, D. Li, *ACS Catal.* **2020**, *10*, 15048–15059; b) A. Garcia-Ortiz, J. D. Vidal, S. Iborra, M. J. Climent, J. Cored, D. Ruano, V. Perez-Dieste, P. Concepcion, A. Corma, *J. Catal.* **2020**, *389*, 706–713.

[9] G. Vilé, D. Albani, M. Nachtegaal, Z. Chen, D. Dontsova, M. Antonietti, N. López, J. Pérez-Ramírez, *Angew. Chem. Int. Ed.* **2015**, *54*, 11265–11269.

[10] a) L. Liu, M. Lopez-Haro, C. W. Lopes, C. Li, P. Concepcion, L. Simonelli, J. J. Calvino, A. Corma, *Nat. Mater.* **2019**, *18*, 866–873; b) Q. Sun, N. Wang, Q. Fan, L. Zeng, A. Mayoral, S. Miao, R. Yang, Z. Jiang, W. Zhou, J. Zhang, T. Zhang, J. Xu, P. Zhang, J. Cheng, D.-C. Yang, R. Jia, L. Li, Q. Zhang, Y. Wang, O. Terasaki, J. Yu, *Angew. Chem. Int. Ed.* **2020**, *59*, 19450–19459; c) N. Wang, Q. Sun, T. Zhang, A. Mayoral, L. Li, X. Zhou, J. Xu, P. Zhang, J. Yu, *J. Am. Chem. Soc.* **2021**, *143*, 6905–6914; d) Q. Chen, P. Peng, G. Yang, Y. Li, M. Han, Y. Tan, C. Zhang, J. Chen, K. Jiang, L. Liu, C. Ye, E. Xing, *Angew. Chem. Int. Ed.* **2022**, *61*, e202205978; e) X. Deng, B. Qin, R. Liu, X. Qin, W. Dai, G. Wu, N. Guan, D. Ma, L. Li, *J. Am. Chem. Soc.* **2021**, *143*, 20898–20906.

[11] a) Z. Jin, L. Wang, E. Zuidema, K. Mondal, M. Zhang, J. Zhang, C. Wang, X. Meng, H. Yang, C. Mesters, F.-S. Xiao, *Science* **2020**, *367*, 193–197; b) J. Zhang, L. Wang, B. Zhang, H. Zhao, U. Kolb, Y. Zhu, L. Liu, Y. Han, G. Wang, C. Wang, D. S. Su, B. C. Gates, F.-S. Xiao, *Nat. Catal.* **2018**, *1*, 540–546.

[12] S. Wang, Z. J. Zhao, X. Chang, J. Zhao, H. Tian, C. Yang, M. Li, Q. Fu, R. Mu, J. Gong, *Angew. Chem. Int. Ed.* **2019**, *58*, 7668–7672.

[13] H. Gökce, S. Bahçeli, *Opt. Spectrosc.* **2013**, *115*, 632–644.

[14] B. Ahmed, D. H. Anjum, M. N. Hedhili, Y. Gogotsi, H. N. Alshareef, *Nanoscale* **2016**, *8*, 7580–7587.

[15] a) H. Munakata, T.-r. Koyama, T. Yashima, N. Asakawa, T. O-Nuki, K. Motokura, A. Miyaji, T. Baba, *J. Phys. Chem. C* **2012**, *116*, 14551–14560; b) E. Dib, J. Grand, S. Mintova, C. Fernandez, *Chem. Mater.* **2015**, *27*, 7577–7579; c) E. Dib, I. M. Costa, G. N. Vayssilov, H. A. Aleksandrov, S. Mintova, *J. Mater. Chem. A* **2021**, *9*, 27347–27352; d) A. B. Fernandez, I. Lezcano-Gonzalez, M. Boronat, T. Blasco, A. Corma, *Phys. Chem. Chem. Phys.* **2009**, *11*, 5134–5141.

[16] a) Q. Sun, B. W. J. Chen, N. Wang, Q. He, A. Chang, C.-M. Yang, H. Asakura, T. Tanaka, M. J. Hulsey, C.-H. Wang, J. Yu, N. Yan, *Angew. Chem. Int. Ed.* **2020**, *59*, 20183–20191; b) D. Childers, A. Saha, N. Schweitzer, R. M. Rioux, J. T. Miller, R. J. Meyer, *ACS Catal.* **2013**, *3*, 2487–2496.

[17] Y. Liu, Z. Liu, Y. Hui, L. Wang, J. Zhang, X. Yi, W. Chen, C. Wang, H. Wang, Y. Qin, L. Song, A. Zheng, F. S. Xiao, *Nat. Commun.* **2023**, *14*, 2531.